Pharmacaeutical Nanotechnology

Design, biometric simulation and optimization of a nano-enabled scaffold device for enhanced delivery of dopamine to the brain

Samantha Pillay [a], Viness Pillay [a,*], Yahya E. Choonara [a], Dinesh Naidoo [b], Riaz A. Khan [c], Lisa C. du Toit [a], Valence M.K. Ndesendo [a], Girish Modi [d], Michael P. Danckwerts [a], Sunny E. Iyuke [e]

[a] University of the Witwatersrand, Department of Pharmacy and Pharmacology, 7 York Road, Parktown 2193, Johannesburg, South Africa
[b] University of the Witwatersrand, Department of Neurosurgery, Division of Neurosciences, 7 York Road, Parktown 2193, Johannesburg, South Africa
[c] Integral University, Department of Industrial Chemistry, Lucknow 226026, India
[d] University of the Witwatersrand, Department of Neurology, Division of Neurosciences, 7 York Road, Parktown 2193, Johannesburg, South Africa
[e] University of the Witwatersrand, School of Chemical and Metallurgical Engineering, Private Bag 3, Wits 2050, Johannesburg, South Africa

ARTICLE INFO

ABSTRACT

This study focused on the design, biometric simulation and optimization of an intracranial nano-enabled scaffold device (NESD) for the site-specific delivery of dopamine (DA) as a strategy to minimize the peripheral side-effects of conventional forms of Parkinson's disease therapy. The NESD was modulated through biometric simulation and computational prototyping to produce a binary crosslinked alginate scaffold embedding stable DA-loaded cellulose acetate phthalate (CAP) nanoparticles optimized in accordance with Box–Behnken statistical designs. The physicomechanical properties of the NESD were characterized and *in vitro* and *in vivo* release studies performed. Prototyping predicted a 3D NESD model with enhanced internal micro-architecture. SEM and TEM revealed spherical, uniform and non-aggregated DA-loaded nanoparticles with the presence of CAP (FTIR bands at 1070, 1242 and 2926 cm^{-1}). An optimum nanoparticle size of 197 nm (PdI = 0.03), a zeta potential of -34.00 mV and a DEE of 63% was obtained. The secondary crosslinker BaCl$_2$ imparted crystallinity resulting in significant thermal shifts between native CAP (T_g = 160–170 °C; T_m = 192 °C) and CAP nanoparticles (T_g = 260 °C; T_m = 268 °C). DA release displayed an initial lag phase of 24 h and peaked after 3 days, maintaining favorable CSF (10 μg/mL) versus systemic concentrations (1–2 μg/mL) over 30 days and above the inherent baseline concentration of DA (1 μg/mL) following implantation in the parenchyma of the frontal lobe of the Sprague–Dawley rat model. The strategy of coupling polymeric scaffold science and nanotechnology enhanced the site-specific delivery of DA from the NESD.

© 2009 Elsevier B.V. All rights reserved.

1. Introduction

Drug delivery to the brain remains a highly challenging and essential field of study. Due to the numerous protective barriers surrounding the Central Nervous System (CNS), there is still an urgent need for the effective treatment of patients living with neurodegenerative disorders such as Parkinson's disease (Singh et al., 2007). Parkinson's disease is one of the most common and severely debilitating neurodegenerative disorders (Hall et al., 2007). It is characterized by a progressive loss of dopamine neurons in the substantia nigra pars compacta of the brain. This results in the loss of striatal dopaminergic terminals and subsequently their inability to store and regulate the release of dopamine. Accord-ingly, striatal dopamine receptor activation becomes increasingly dependent on the peripheral availability of an exogenously admin-istered dopaminergic agent (Marin et al., 2008). As the disease progresses, the patient begins to experience motor abnormalities such as akinesia, resting tremor, and rigidity. The advancement of the disease results in worsening of these symptoms. The blood–brain barrier (BBB) is a defensive mechanism and there-fore the passage of substances into the brain is highly selective. This is a major impediment for drug delivery to the brain as numerous neuroactive drugs are aqueous in nature and therefore unable to penetrate the BBB (Elkharraz et al., 2006). Drugs may be delivered systemically as is the case with current drug ther-apy. However, only a small percentage of drugs reach the brain due to hepatic degradation, and the associated peripheral side-effects related to peak-to-trough fluctuation of plasma levels of drug leads to a lack in patient dose-regimen compliance (Whitney, 2007).

Currently, levodopa, the levorotatory isomer of dihydroxy-phenylalanine, a metabolic precursor of dopamine is the main therapy used for the treatment of Parkinson's disease. Levodopa is converted into dopamine in the basal ganglia and the current widespread use of levodopa is to enhance its transport across the BBB. Initial therapy with levodopa significantly restores the normal functioning of a patient with Parkinson's disease (Samii et al., 2004). However a major limitation to the chronic use of levodopa from conventional oral dosage forms is the resultant 'end-of-dose wearing-off' effect where the therapeutic efficacy of each dose of levodopa resides for shorter periods (Hely et al., 2000). Hence, the patient begins to experience motor fluctuations prior to the next dose and therefore the initially prescribed dose is no longer able to effectively manage the symptoms of the disease such as pain, panic attacks, severe depression, confusion and a sense of impending death (Papapetropoulos and Mash, 2005). Clinicians attempt to overcome this phenomenon by increasing the frequency or quantity of the dose via substituting from immediate release to sustained-release oral formulations to overcome "the wearing-off" effect such as Sinemet® CR (Merck & Co. Inc., Whitehouse Station, NJ, USA). However, an increased dosing frequency places the patient at a risk of developing side-effects such as dyskinesias (Uitti et al., 1997; Chen and Obering, 2005). Furthermore, the inclusion of carbidopa with levodopa tends to exacerbate psychiatric, gastrointestinal and motor side-effects (Roos et al., 1993; Pahwa and Koller, 1998).

Polymeric nanotechnology has been investigated for application in targeted cancer therapy (Bilensoy, 2007). However, there has been minimal progress in the design and institution of nanotechnology for the site-specific treatment of neurodegenerative disorders. Therefore this work explored the design and development of a biodegradable nano-enabled scaffold device (NESD) to be implanted into the parenchyma of the frontal lobe of the brain in order to target the delivery of dopamine for the chronic management of Parkinson's disease. Dopamine was employed as the model drug incorporated within stable polymeric nanoparticles and thus the peripheral conversion to dopamine that leads to numerous side-effects would be avoided as noted with conventional oral levodopa delivery systems. The NESD is envisaged to simplify the treatment of Parkinson's disease, maintain therapeutic levels of dopamine within the brain, reduce the extensive peripheral side-effects experienced by patients and decrease the quantity of dopamine needed as well as the dosing frequency. The inclusion of cellulose acetate phthalate (CAP) nanoparticles into a binary crosslinked alginate scaffold would facilitate the controlled delivery of dopamine and avail higher drug-loading capacities due to the larger surface area to volume ratio (Ahmad and Khan, 2005).

In addition, prototyping technology has created a significant impact in biomedical materials design. Molecular modeling facilitates the design of accurately customized structural models of polymeric devices for various applications (Levy et al., 1997; Ono et al., 1999; Chua et al., 2000; Curodeau et al., 2000; Porter et al., 2001; Cheah et al., 2002; Discher et al., 2007). Therefore, this has prompted us to adopt a similar approach to fabricate the NESD with controlled micro-architecture and higher consistency than conventional non-computerized techniques that rely solely on individual intervention. Computer-aided free-form prototyping technology was used to design the NESD via a three-dimensional (3D) crosslinked alginate scaffold model incorporating CAP nanoparticles. Prototyping provided an approach that aimed to improve the NESD design by employing archetype data manipulation to pre-assemble the complex internal scaffold architectures and nanostructures of the NESD in conjunction with Box–Behnken statistical experimental designs for optimization and an integrated corporeal manufacturing approach that is consistent, reproducible and formulation-specific.

2. Materials and methods

2.1. Materials

Alginate (Protanal® LF10/60; 30% mannuronic acid, 70% guluronic acid residues) was purchased from FMC Biopolymer (Drammen, Norway). Calcium gluconate [(HOCH$_2$(CHOH)$_4$COO)$_2$Ca], barium chloride (BaCl$_2$), cellulose acetate phthalate (CAP) (M_w = 49,000 g/mol), poly(vinyl alcohol) (PVA), acetone, methanol and dopamine hydrochloride (DA) (M_w = 189.64 g/mol) were purchased from Sigma–Aldrich (St. Louise, MO, USA). Double deionized water was obtained from a Milli-Q water purification system (Milli-Q, Millipore, Billerica, MA, USA). Solid phase extraction procedures were performed with Oasis® HLB cartridges purchased from Waters® (Milford, MA, USA). Healthy adult Sprague–Dawley rats were used for the in vivo release study. Theophylline was used as an internal standard during UPLC analysis. All solvents used for UPLC analysis were of superior analytical grade.

2.2. Computer-aided prototyping of the nano-enabled scaffold device

Computer-aided design employs information technology to design, develop and optimize a desired system. The usefulness, with specific reference to this investigation where a number of device components were implicated in the design of the nano-enabled scaffold device (NESD), was derived from the knowledge obtained relating to the molecular structure which was intrinsic to the modus operandi of the NESD device. The implicit design of the NESD required customization of the crosslinked alginate scaffold for embedding the DA-loaded CAP nanoparticles with the ability to support bioadhesion and the physicomechanical stability on a molecular basis for intracranial implantation of the device. CAP and [(HOCH$_2$(CHOH)$_4$COO)$_2$Ca]-crosslinked alginate were selected for producing the nanoparticles and scaffold components of the NESD respectively. The crosslinked scaffold was subsequently cured in a BaCl$_2$ solution as a secondary crosslinking step. The componential NESD properties were modulated through computational prototyping to produce a viable scaffold embedded with stable CAP nanoparticles. The fundamental design parameters were pivoted on the polymer assemblage, curing methods, surface properties, macrostructure, physicomechanical properties, nanoparticle fixation and biodegradation of the NESD. In order to incorporate fine control within the complexities of three-dimensional (3D) design, the physical properties of the crosslinked alginate scaffold such as the pore size, shape, wall thickness, interconnectivity and networks for nanoparticle diffusion was regulated to produce a 3D prototype NESD model. The NESD topography was predicted for intracranial implantation with pre-defined micro-architecture and physicomechanical properties equilibrating the frontal lobe parenchyma of the brain as the site of device implantation to provide mechanical support during sterilization prior to function. A suppositional 3D graphical model with potential inter-polymeric interactions during formation was generated on ACD/I-Lab, V12 Structure Elucidator Application (Add-on) biometric software (Advanced Chemistry Development Inc., Toronto, Canada, 2009) based on the step-wise molecular mechanisms of scaffold and nanoparticle formation, polymer interconversion and DA-loaded nanoparticle fixation as envisioned by the chemical behavior and physical stability. A combination of a computationally rapid Neural Network (NN) and a modified Hierarchal Organization of Spherical Environments (HOSE) code approach were employed as the fundamental algorithms in designing the prototype NESD. The associated energy expressions were chemometrically designed based on the assumption of the scaffold behaving initially as a gel-like structure with higher states of combinatory energy for the complete NESD.

Table 1
Independent formulation variables and responses selected for NESD preparation and optimization.

Independent variables	Levels		Objective
	Lower	Upper	
Crosslinked alginate scaffold			
Alginate (% w/v)	1	3	
Calcium gluconate (%, w/v)	0.2	0.6	
Temperature (°C)	50	70	
Post-curing time (min)	30	90	
Responses			
Matrix Resilience (%)	86	94	Maximize
Matrix Erosion (%)	3	59	Minimize
DA-loaded CAP nanoparticles			
CAP (g)	0.5	1	
PVA (%, w/v)	0.5	2	
Stirring speed (rpm)	300	700	
Emulsifying time (min)	30	180	
Responses			
Mean dissolution time (MDT)	38		Maximize
Zeta potential (mV)	−20		Maximize
Particle size (nm)	150		Minimize

2.3. Box–Behnken experimental design strategies for NESD preparation and optimization

The Box–Behnken design was employed for the generation of quadratic response surfaces and construction of second order polynomial models for the prediction of the NESD behavior in terms of the independent variables investigated. This facilitated a mechanistic evaluation of possible correlations between pertinent processing factors implicated in nanoparticle- and scaffold-design. Two separate quadratic 4-factor Box–Behnken statistical experimental designs were constructed in order to produce concise experimental batches of the crosslinked alginate scaffold and DA-loaded CAP nanoparticles as the solitary components of the NESD. The scaffold for implantation is intended to remain intact (over a period of at least 30 days for experimentation purposes) and resist micromechanical transitions upon hydration. On release of the DA-loaded CAP nanoparticles from the polymeric platform, they are anticipated to exhibit enhanced release of DA directly at the site of implantation and demonstrate a desirable size range for diffusion through the porous network of the scaffold. Based on these design parameters, the scaffold and CAP nanoparticles were optimized within each design matrix in constraints of maximizing the scaffold Matrix Resilience in the hydrated state to ensure maintenance of NESD integrity, and minimizing the scaffold matrix erosion to provide a constant environment for nanoparticle diffusion. The mean dissolution time (MDT) of DA from the CAP nanoparticles was maximized to ensure the establishment and maintenance of adequate DA levels, and the particle size of the CAP nanoparticles was minimized in alignment with the pore size of the alginate scaffold to facilitate nanoparticle diffusion through the porous matrix. The lower and upper boundaries of the independent formulation factors, the responses selected and the optimization constraints for the crosslinked alginate scaffold and CAP nanoparticles are listed in Table 1. Quadratic relationships linking the independent formulation factors and responses were generated, and the components of the NESD were optimized under pre-determined constraints intimated by the initial prototyping technology employed. The study design was generated and analyzed using Minitab® V15 software (Minitab® Inc., PA, USA) with two separate formulation design templates for the crosslinked alginate scaffold and CAP nanoparticles with a total of 27 experimental runs for each blueprint.

2.4. Corporeal assembly of the NESD

Production of the NESD device required the initial componential preparation and optimization of the crosslinked alginate scaffold and the DA-loaded CAP nanoparticles. Once the two components were optimized the DA-loaded CAP nanoparticles were incorporated via intermittent blending and lyo-fusion (spontaneous freezing followed by lyophilization) into the $[(HOCH_2(CHOH)_4COO)_2Ca]$-crosslinked and $BaCl_2$-cured alginate scaffold.

2.4.1. Preparation of the crosslinked alginate scaffold

A 2% (w/v) alginate solution in deionized water (Milli-DI® Systems, Bedford, MA, USA) was prepared at 50 °C and a primary 0.4% (w/v) $[HOCH_2(CHOH)_4COO]_2Ca$ crosslinking solution was added and agitated until a homogenous mixture was obtained. The resulting 'gel-like' solution was then placed in Teflon moulds and lyophilized for 24 h at 25 mTorr. Thereafter the lyophilized structures were immersed in a secondary 2% (w/v) $BaCl_2$ crosslinking solution for 3 h as a curing step followed by a further lyophilization phase of 24 h at 25 mTorr (Virtis®, Gardiner, NY, USA). The resultant cured scaffolds were removed from the moulds, washed with $3× 100$ mL deionized water in order to leach out any unincorporated salts and air-dried under an extractor until a constant mass was achieved. All formulations were prepared in accordance with a Box–Behnken experimental design template (Table 2).

2.4.2. Preparation of the DA-loaded CAP nanoparticles

Nanoparticles were prepared using an adapted emulsification-diffusion technique (Piñón-Segundo et al., 2005) in accordance with a Box–Behnken experimental design template generated (Table 3). Briefly, 500 mg of CAP and 50 mg of DA were dissolved in a binary solvent system of acetone and methanol in a 3:7 ratio (100 mL). A 1% (w/v) PVA solution was then added as a surfactant. The solution was agitated for 30 min using a magnetic stirrer set at 700 rpm. A sub-micronized o/w emulsion was spontaneously formed due to immediate reduction of the interfacial tension with rapid diffusion of the binary organic solvent system into the aqueous phase known as the Marangoni Effect (Poletto et al., 2008). Excess solvent was evaporated using a rotavap (Rotavapor® RII, Büchi Labortechnik AG, Flawil, Switzerland) maintained at 60 °C for 1 h and the resulting concentrate was centrifuged (Optima® LE-80K, Beckman, USA) at 20,000 rpm for 20 min. The sedimentary layer containing CAP nanoparticles was then removed and lyophilized for 24 h at 25 mTorr to obtain a free-flowing powder for incorporation into the crosslinked alginate scaffold via lyo-fusion.

2.4.3. Assimilation of the crosslinked scaffold and CAP nanoparticles into the NESD

The NESD was assembled by a lyo-fusion process. Briefly, the optimally defined DA-loaded CAP nanoparticles (200 mg) were placed into moulds containing a $[HOCH_2(CHOH)_4COO]_2Ca$-alginate solution (2 mL) obtained in accordance with set optimization constraints. The mixture was agitated and spontaneously frozen at −70 °C for 24 h. The frozen structures were lyophilized for 48 h at 25 mTorr and thereafter immersed in a 2% (w/v) $BaCl_2$ crosslinking solution for 3 h as a curing step followed by a further lyophilization phase of 24 h at 25 mTorr to induce fusion of the DA-loaded CAP nanoparticles and the crosslinked and cured alginate scaffold.

2.5. Determination of particle size and zeta potential

In order to assess the physical stability of the DA-loaded CAP nanoparticles produced, the zeta potential value was analyzed using a Zetasizer NanoZS instrument (Malvern Instruments (Pty) Ltd., Worcestershire, UK) to measure the particle surface charge.

Table 2
Box–Behnken experimental design template generated for producing the crosslinked alginate scaffold.

Formulation number	[Alginate] (%, w/v)	Process temperature (°C)	[Crosslinker] (%, w/v)	Post-curing time (min)
1	3	60	0.2	60
2	3	60	0.6	60
3	2	50	0.6	60
4	2	60	0.4	60
5	2	60	0.6	30
6	3	60	0.4	30
7	2	60	0.4	60
8	2	50	0.4	90
9	1	50	0.4	60
10	2	60	0.4	60
11	1	60	0.4	90
12	2	60	0.2	90
13	2	60	0.6	90
14	1	70	0.4	60
15	1	60	0.4	30
16	2	70	0.4	90
17	3	70	0.4	60
18	2	70	0.4	30
19	1	60	0.2	60
20	2	70	0.2	60
21	3	50	0.4	60
22	2	50	0.2	60
23	3	60	0.4	90
24	2	50	0.4	30
25	1	60	0.6	60
26	2	60	0.2	30
27	2	70	0.6	60

Table 3
Box–Behnken experimental design template generated for producing the DA-loaded CAP nanoparticles.

Formulation number	[CAP] (%, w/v)	[PVA] (%, w/v)	Emulsifying time (min)	Stirring speed (rpm)
1	1.00	1.25	30	500
2	1.00	1.25	180	500
3	0.75	0.50	180	500
4	0.75	1.25	105	500
5	0.75	1.25	180	300
6	1.00	1.25	105	300
7	0.75	1.25	105	500
8	0.75	0.50	105	700
9	0.50	0.50	105	500
10	0.75	1.25	105	500
11	0.50	1.25	105	700
12	0.75	1.25	30	700
13	0.75	1.25	180	700
14	0.50	2.00	105	500
15	0.50	1.25	105	300
16	0.75	2.00	105	700
17	1.00	2.00	105	500
18	0.75	2.00	105	300
19	0.50	1.25	30	500
20	0.75	2.00	30	500
21	1.00	0.50	105	500
22	0.75	0.50	30	500
23	1.00	1.25	105	700
24	0.75	0.50	105	300
25	0.50	1.25	180	500
26	0.75	1.25	30	300
27	0.75	2.00	180	500

DA-loaded CAP nanoparticle samples (1%, w/v) produced in accordance with the Box–Behnken formulation design template were appropriately suspended in deionized water as the dispersant, passed through a membrane filter (0.22 μm, Millipore Corp., Bedford, MA, USA) to maintain the number of counts per second in the region of 600, and placed into folded capillary cells. The viscosity and refractive index of the continuous phase were set to those specific to deionized water. Particle size measurements were performed in the same manner using quartz cuvettes. Measurements were taken in triplicate with multiple iterations for each run in order to elute size intensity and zeta potential distribution profiles over time.

2.6. Assessment of drug entrapment efficiency of the CAP nanoparticles

In order to assess the entrapment efficiency of DA within the CAP nanoparticles, various polymer:drug ratios were considered (ranging from 5:1 to 10:1) and post-lyophilized powdered samples were accurately weighed and completely dissolved in phosphate-

buffered saline (PBS) (pH 6.8; 37 °C). The DA content was analyzed by UV spectrophotometry at $\lambda_{280\,nm}$ (Hewlett Packard 8453 Spectrophotometer, Germany) and computed from a standard linear curve of DA in PBS (pH 6.8; 37 °C) ($R^2 = 0.99$). No interference was noted from polymeric absorbance with the UV assay method developed. Eq. (1) was utilized to compute the drug entrapment efficiency (DEE).

$$DEE\% = \frac{D_a}{D_t} \times 100 \tag{1}$$

where *DEE%* is the drug entrapment efficiency, D_a is the actual quantity of DA (mg) measured by UV spectroscopy and D_t is the theoretical quantity of DA (mg) added in the formulation.

2.7. Morphological characterization of the NESD

Morphological characterization of the crosslinked alginate scaffold and DA-loaded CAP nanoparticles was instituted. The shape, size homogeneity and possible degree of aggregation were identified for the DA-loaded and native CAP nanoparticles. In addition the scaffold parameters such as the micro-structure pore length, pore distribution and inter-pore wall thickness was also examined. The surface morphology of the cured and un-cured crosslinked alginate scaffolds were also characterized to assess the influence of crosslinking and subsequent curing on potential surface morphological transitions ($N = 10$). Scanning Electron Microscopy (SEM) (JOEL, SEM 840, Tokyo, Japan) was employed and photomicrographs were captured at various magnifications for analyzing the scaffold and CAP nanoparticle samples that were prepared after sputter-coating with carbon. The particle size and shape was also explored using Transmission Electron Microscopy (TEM) (JEOL 1200 EX, 120 keV TEM, Tokyo, Japan) for higher definition and resolution. Samples were prepared by placing a dispersion of the CAP nanoparticles in ethanol on a copper grid with a perforated carbon film followed by evaporation and viewing at room temperature ($N = 10$).

2.8. Physicomechanical characterization of the crosslinked alginate scaffold

One of the key approaches to intricate crosslinked polymeric scaffold engineering is the assessment of the physicomechanical properties of the scaffold matrix following 3D prototyping and prior to sterilization and intracranial implantation. The micromechanical properties of the crosslinked alginate scaffold may directly influence the ability of the CAP nanoparticles to fuse and migrate during preparation, sterilization and function. Textural profile analysis was therefore conducted to characterize the 3D salient core regions of the crosslinked alginate scaffold using a Texture Analyzer (TA.XT*plus* Stable Microsystems, Surrey, UK) in terms of the scaffold Matrix Resilience. Hydrated samples of the crosslinked alginate scaffold were analyzed. Serial Force–Time profiles were sufficient to perform the necessary computations of Matrix Resilience ($N = 5$). The parameter settings employed comprised a Pre-Test Speed = 1.0 mm/s, a Test Speed and Post-Test Speed = 1.5 mm/s, 50% strain under a Compressive Test Mode with a Trigger Force of 0.05 N.

2.9. Determination of polymeric structural variations due to CAP nanoparticle formation

The molecular structure of native CAP, DA, the DA-free and DA-loaded CAP nanoparticles, and the nanoparticle-free and nanoparticle-loaded NESD produced were analyzed using Fourier Transmission Infrared (FTIR) spectroscopy to elucidate any variations in vibrational frequencies and subsequent polymeric

structure as a result of DA–CAP interaction during nanoparticle formation. Molecular structural changes in the CAP backbone may alter the inherent chain stability and therefore affect the physicochemical and physicomechanical properties of the selected polymer type for the intended purpose. Samples were blended with potassium bromide (KBr) in a 1% (w/w) ratio and compressed into 1 mm × 13 mm disks using a Beckmann Hydraulic Press (Beckman Instruments Inc., Fullerton, USA) set at 8 t. The sample disks were analyzed in triplicate at high resolution with wavenumbers ranging from 4000 to 400 cm^{-1} on a Nicolet Impact 400D FTIR Spectrophotometer coupled with Omnic FTIR research grade software (Nicolet Instrument Corp., Madison, WI, USA).

2.10. Componential thermal characterization of the NESD

The inherent and sequential transient thermal behavior of polymers may influence the physicochemical and physicomechanical properties as well as the final performance of the system (Liu et al., 2003). Temperature Modulated Differential Scanning Calorimetry (TMDSC) was therefore performed to provide a distinct interpretation of the polymeric thermal transitions with improved sensitivity and the ability to separate reversible glass transition temperatures (T_g) that have minimal changes in heat capacity (ΔH) from overlapping non-reversible relaxation endotherms (Reading, 1993; Ferrero et al., 1999; Sandor et al., 2002). Thermal analysis was therefore undertaken on the DA-loaded CAP nanoparticles, the crosslinked alginate scaffold and the assimilated NESD in order to assess thermal behavior using TMDSC (Mettler Toledo DSC1 STAR^e System, Switzerland). Thermal transitions were assessed in terms of the T_g, measured as the reversible heat flow due to variation in the magnitude of the C_p-complex values (ΔC_p); melting temperature (T_m) and crystallization temperature (T_c) peaks that were consequences of irreversible heat flow corresponding to the total heat flow. The temperature calibration was accomplished with a melting transition of 6.7 mg indium. The thermal transitions of native CAP were compared to the CAP nanoparticles. Samples of 5 mg were weighed in perforated 40 μL aluminum pans and ramped within a temperature gradient of 150–500 °C under a constant purge of N$_2$ atmosphere in order to diminish oxidation. The instrument parameter settings employed comprised a sine segment starting at 150 °C with a heating rate of 1 °C/min at an amplitude of 0.8 °C and a loop segment incremented at 0.8 °C and ending at 500 °C.

2.11. In vitro assessment of the matrix erosion of the crosslinked alginate scaffold

Samples of the biodegradable crosslinked alginate scaffolds were immersed in 100 mL phosphate-buffered saline (PBS) (pH 6.8, 37 °C) and agitated at 20 rpm in a shaking incubator (Labex Stuart SBS40®, Gauteng, South Africa). At pre-determined time intervals samples were removed, blotted on filter paper and dried to a constant mass at 40 °C in a laboratory oven. Eq. (2) was then used to compute the extent of Matrix Erosion after gravimetrical analysis.

$$ME\% = \frac{M_0 - M_t}{M_0} \times 100 \tag{2}$$

where *ME%* is the extent of scaffold Matrix Erosion, M_t is the mass of the scaffold at time t and M_0 is the initial mass of the scaffold.

2.12. In vitro DA release from the CAP nanoparticles and the NESD

In vitro release studies were performed on the DA-loaded CAP nanoparticle formulations and the final NESD utilizing a shaking incubator (Labex, Stuart SBS40®, Gauteng, South Africa) set at 20 rpm. The DA-loaded CAP nanoparticles and NESD were immersed separately in 100 mL phosphate-buffered saline (PBS)

(pH 6.8, 37 °C) contained in 150 mL sealed glass vessels. At pre-determine time intervals 3 mL samples of each release media were removed, filtered through a 0.22 μm cameo acetate membrane filter (Millipore Co., Bedford, MA, USA) and centrifuged at 20,000 rpm (Redhead et al., 2001). The supernatant was then removed and analyzed by UV spectroscopy at a maximum wavelength of $\lambda_{280\,nm}$ for DA content analysis. There was no interference noted from polymeric absorbance with the UV assay method developed. DA release was quantified using a linear standard curve ($R^2 = 0.99$). An equal volume of DA-free PBS was replaced into the release media to maintain sink conditions. The mean dissolution time (MDT) values were calculated at 8 h for each sample using Eq. (3). Computing the release data in this manner allowed for the effective model-independent comparison of all formulations in terms of their respective DA release behavior. All release studies were performed in triplicate.

$$MDT = \sum_{i=1}^{n} t_i \frac{M_t}{M_\infty} \tag{3}$$

where M_t is the fraction of dose released in time $t_i = (t_i + t_{i-1})/2$ and M_∞ corresponds to the loading dose.

2.13. In vivo analysis of DA release from the NESD in a Sprague–Dawley rat model

Forty-five adult male Sprague–Dawley rats weighing 350 ± 20 g (having an approximate brain volume of 865 cm^3) were used to perform the *in vivo* study for implantation of the NESD into the parenchyma of the frontal lobe. Baseline plasma samples were taken and rats were anesthetized with a mixture of ketamine (65 mg/kg) and xylazine (7.5 mg/kg) before being placed in a Kopf stereotaxic frame. A straight midline incision (5–10 mm) was made from nasion to occiput. The skin and periosteum was reflected exposing the dorsal surface of the skull in order to facilitate identification of the cranial sutures and to ensure the skull trephination was made in the frontal bone. A surgical drill was then used to produce a controlled perforation of the skull with an opening of approximately 0.5 mm in diameter followed by sharp incision of the dural lining. The brain parenchyma was then ready for insertion of the NESD. The cylindrically shaped NESD was scaled to 0.04% of the rat brain volume (0.000354 cm^3 versus 0.865 ± 0.026 cm^3) that was equivalent to an actual size of the NESD device being significantly <20% of adult human brain volume. The wound was sealed with wax and the scalp insertion was closed with a single layer of non-absorbable suture. Temgesic (1 mL) was administered post-operatively for pain relief with a rehydration treatment of 5% glucose in 0.9% saline and a series of behavioral asymmetry tests were performed on the rats to assess any degree of motor dysfunction present.

At days 0, 3, 7, 14, 21 and 30 post-implantation, the animals were anaesthetized and blood samples (2.5 mL) were collected via cardiac puncture, as well as 20 μL of cerebrospinal fluid (CSF). A sampling volume of 20 μL was selected in order to be representative of brain CSF as larger volumes of CSF would result in aspiration from more distant spinal regions of the CNS. The CSF was aspirated through puncturing the cisternal magna and gently withdrawing CSF fluid through a 30G needle and micro-syringe attached to specialized polyethylene tubing. The rats were subsequently euthanized with an overdose of sodium pentobarbitone. All plasma and CSF samples were stored at −70 °C prior to Ultra Performance Liquid Chromatography (UPLC) analysis. A standard curve of DA in blank plasma was generated from a primary stock aqueous solution of DA (100 mg/mL) and serially diluted to obtain concentrations ranging from 0.0016 to 30.00 μg/mL. Theophylline was used as the internal standard. Plasma and CSF samples were thawed and ace-

tonitrile (0.4 mL) was added to each sample for deproteinization and centrifuged (Optima® LE-80K, Beckman, USA) at 15000 rpm for 10 min. The supernatant was removed and subjected to a generic Oasis® HLB Solid Phase Extraction (SPE) procedure and placed in Waters® certified UPLC vials (1.5 mL). UPLC analysis was performed on an Acquity® Ultra Performance Liquid Chromatography system (Waters®, Milford, MA, USA) coupled with a PDA detector. Separation was achieved on an Acquity® UPLC BEH C$_{18}$ column (50 mm × 2.1 mm, 1.7 μm particle size) maintained at 25 °C. Samples were injected with an injection volume of 3.7 μL at a flow-rate of 0.5 mL/min and a run-time of 2 min. A binary mobile phase was used comprising 98% 0.1 M ammonium acetate of pH 5.0 and 2% acetonitrile.

3. Results and discussion

3.1. Computer-aided prototyping for NESD design

Prototyping was undertaken for the purpose of gaining an in-depth definition of the molecular basis underlying the functionality of the NESD. An output format of several serial bitmap images generated via prototyping technology enabled the step-wise 3D volumetric construction of the NESD model. 3D construction was initiated by ascribing an assumed height to each image in order to represent a volume unit or a stacked voxel depicting an optimized prototype model of the NESD described by the grayscale intensity threshold images shown in Fig. 1. Prototyping of the NESD device confirmed that the functional properties of the NESD depended on the characteristics of the polymeric materials employed, the processing technique, and the subsequent interaction of fixated CAP nanoparticles within the crosslinked alginate scaffold. The 3D prototype design of the device permitted the porosity (mean pore size = 100–500 μm), surface area ($A = 0.0004$ cm^3), and surface characteristics to be semi-optimized in the pre-cured and post-cured phases with BaCl$_2$ for each component of the NESD (Fig. 1a). Fine control of the micro-architectural characteristics influenced the mechanical properties of the scaffold that was significant for CAP nanoparticle fixation and mechano-transduction in order to control the release of DA. A significant advantage of employing prototyping technology to develop the NESD was the elimination of reliance on individual skills that are required for conventional techniques of device fabrication. In addition, initial prototyping aided in predicting the dependant formulation variable boundaries required for constructing the Box–Behnken experimental design templates for each of the NESD components. Commencing with a limited range of fundamental structural units a NESD with precise micro-architecture was designed using prototyping technology with internal channels or cavities resembling the negative image of the final required NESD as depicted in Fig. 1a–c. Visibly, the scaffold models depicted channels that extended through the entirety of the tetragon matrices in both horizontal and vertical axes with consistency in the strand layout after DA-loaded CAP nanoparticle fixation. At the periphery of the matrix, a region of substantial and blurred pore deposition was visible after curing the alginate scaffold in BaCl$_2$ (Fig. 1b). This entire matrix region was approximately 5 mm × 3 mm at the edge of the tetragon (Fig. 1 enlarged for clarity). SEM images confirmed the strut and pore widths to be in the range of 100–400 μm. Furthermore, the unconnected pore space, when inspected qualitatively, comprised diminutive cavities within the matrix for allowing the outward diffusion of the DA-loaded CAP nanoparticles from the crosslinked alginate scaffold.

The computational design process also revealed that curing of the crosslinked alginate scaffold in BaCl$_2$ involved the residual crosslinking of open, approachable and chemically reactive molecular functional groups that possessed chemical affinity towards
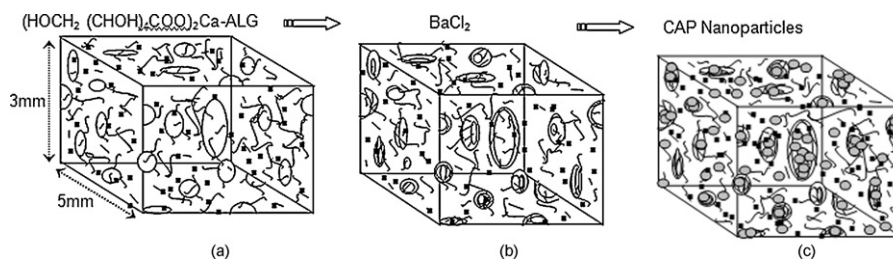
Fig. 1. Three-dimensional prototype images of (a) a pre-cured crosslinked alginate scaffold, (b) a $BaCl_2$ post-cured crosslinked alginate scaffold, and (c) DA-loaded CAP nanoparticles embedded within the cured crosslinked alginate scaffold voids representing the NESD.
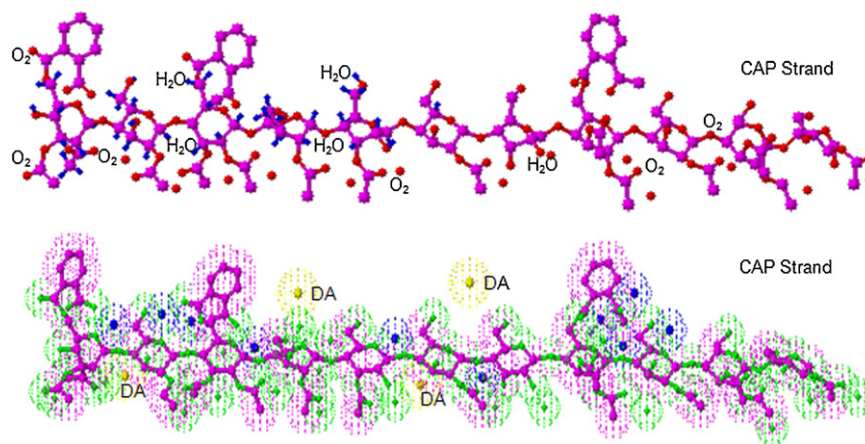

Fig. 2. Molecular structural models of (a) interactions between H_2O molecules in association with acetate and O_2 functional groups of CAP and (b) CAP interactions and DA entrapment.

$BaCl_2$ as the secondary crosslinker and produced an equivalent of edging and interlocking of the matrix surface functional groups with a superiorly compact matrix structure (Fig. 1b), i.e. ionotropic crosslinking of the carboxylic functional groups of alginate by Ba^{2+} cations. Furthermore DA was not covalently bonded to the CAP with no amide bond formation but interacted ionically via physical associations involving H-bonding and smaller force interactions through the influence of the external crosslinking medium. Fig. 2a represents a structural model of the interactions between H_2O molecules in association with acetate and O_2 functional groups of strongly hydrophilic CAP sites. DA as well as other ionic and molecular species revealing an interactive model of CAP and DA entrapment constituents is also depicted in Fig. 2b.

Fig. 3a–e depicts a step-wise single CAP chain structural model under the influence of surrounding interactive forces within the emulsified medium, such as solvent molecules at the periphery, PVA as the surfactant and DA. The affinity interactions with explicit lipophilic and hydrophilic orientations towards the formation of a nanoparticle wall are also shown (Fig. 3f–h). CAP was initially suspended in the binary acetone:methanol solvent system as unorganized random orientations with irregular lipophilic rings (Fig. 3a). The addition of DA and ionic or physical interactions with the hydrophilic functional groups of CAP and free DA molecules resulted in CAP conforming to orientations of the affinity-wise molecular sites in terms of lipophilicity and hydrophilicity of the medium (Fig. 3b). DA also influenced the overall polarity spec-
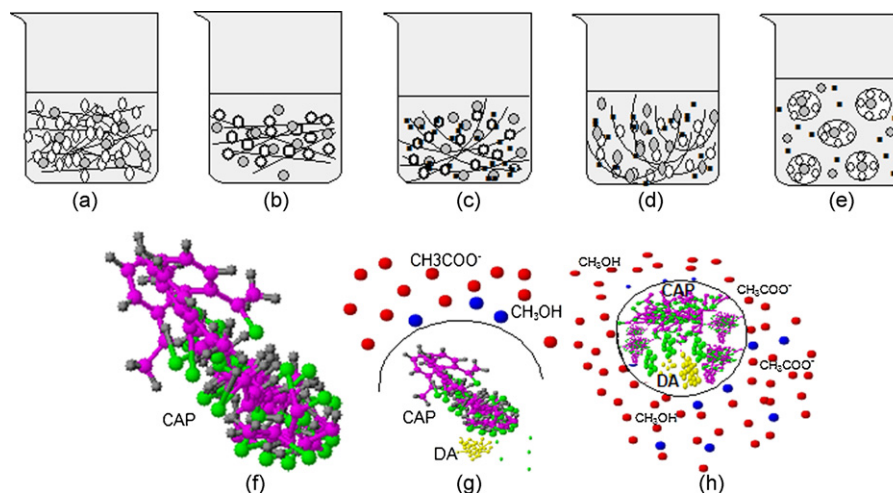

Fig. 3. Graphical models depicting (a–e) the step-wise formation of DA-loaded CAP nanoparticles, (f) a single CAP adaptation, (g) DA interaction and wall initiation and (h) a DA-loaded CAP nanoparticle towards completion.
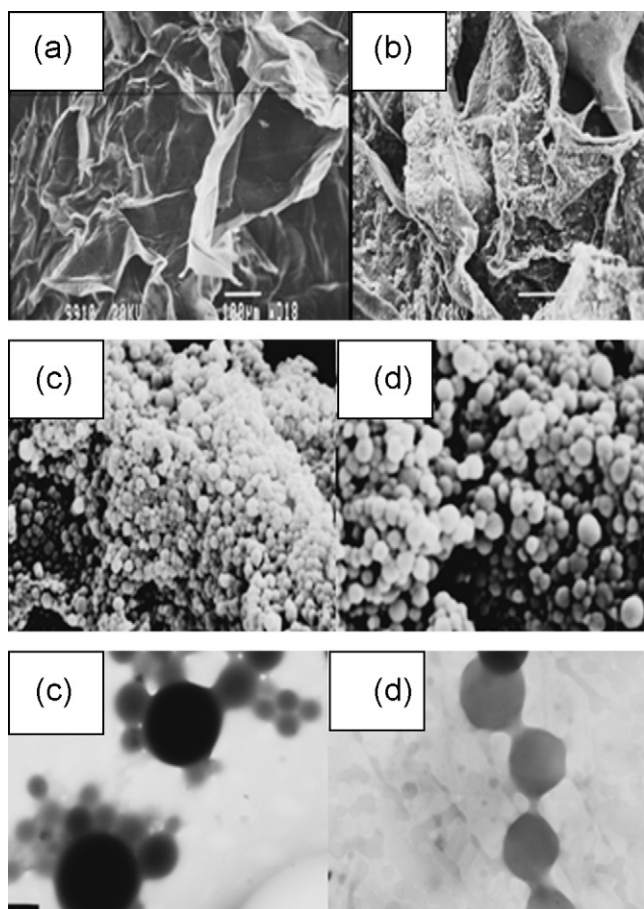
Fig. 4. SEM images (1 mm = 0.5 μm) of a BaCl$_2$ (a) un-cured and (b) cured crosslinked alginate scaffold surface, (c) DA-free nanoparticles, (d) DA-loaded nanoparticles, and TEM images (1 mm = 40 nm) of (e) DA-free nanoparticles and (f) DA-loaded nanoparticles.

trum of the medium. The addition of PVA as a surfactant produced strong molecular associations and crosslinker ions with the subsequent energy supplied via agitation and processing temperatures contributing to surface interactions that produced CAP molecules pivoted toward surface minimization, compactness and orientations of the lipophilic regions (Fig. 3c). The stronger energetic orientations and the presence of PVA as the surfactant tended to promote aggregation of the CAP strands into spheres (Fig. 3d). The CAP strands were completely engaged in sphere formation to produce CAP nanoparticles under the primary influence of solvent diffusion phenomena and the presence of PVA with the inner core containing DA molecules and lipophilic regions of CAP conforming toward the periphery as the boundary between the outer hydrophilic medium (Fig. 3e). Thus, DA molecules orientated within the hydrophilic voids of the CAP nanoparticles shielded by the lipophilic boundary to form stable CAP nanoparticles.

3.2. Morphological characterization of the crosslinked scaffold and CAP nanoparticles

As stated, the crosslinked alginate scaffold displayed an average pore size of 100–400 μm with a wall thickness calculated at an average of 10 ± 1.04 μm. This pore size was anticipated to allow for the efficient diffusion and release of CAP nanoparticles within the crosslinked scaffold micro-architecture. Scaffolds that were not subjected to post-curing in a secondary crosslinking BaCl$_2$ solution revealed a "tissue-like" appearance (Fig. 4a) in comparison to the

evenly distributed porous crystalline yet compact appearance of post-cured scaffolds (Fig. 4b).

SEM images of the CAP nanoparticles depicted the presence of exemplary particles in both DA-free and DA-loaded states (Fig. 4c and d). The spherical particles were uniform in size with a distinct non-aggregated architecture. TEM images of DA-free particles revealed opaque structures with variations in size (Fig. 4e). DA-loaded CAP nanoparticles were slightly transparent with a degree of transient aggregation (Fig. 4f). Overall both DA-free and DA-loaded CAP nanoparticles displayed patent surface morphologies. The thickness of the scaffold diffusion layer was monitored by high-field stereo-microscopy. Due to the minimal swelling of the scaffold (as a result of the HCl-cured crosslinked alginate) a significant transition in the diffusion layer thickness was not detected.

3.3. Polymeric molecular structure variation analysis due to CAP nanoparticle formation

FTIR spectra (not shown) for DA-free nanoparticles revealed a broad stretch band (1070–1242 and 3200–3600 cm^{-1}) representing OH$^-$ groups and a stretch band (2926 cm^{-1}) indicating alkane moieties while a band at 1731 cm^{-1} revealed the presence of –C=O within the CAP nanoparticle structure. The interpretation demonstrates the definitive presence of impervious CAP in DA-free nanoparticles. The spectra for DA-loaded CAP nanoparticles also confirmed the presence of CAP (bands at 1070, 1242 and 2926 cm^{-1}) while the possible interaction of CAP OH$^-$ functional groups with the –NH$_2$ group of DA may have resulted in the formation of nitro compounds (1390 cm^{-1}). The interaction between the H$^+$ of the NH$_2$ group on DA and the O$^-$ atom of the OH$^-$ group on CAP may have culminated in the proposed physical interactions of the two compounds retarding DA release as predicted initially via the prototyping technology employed. There was no notable interaction between the CAP as nanoparticles and the alginate scaffold, implying that release of the CAP nanoparticles from the NESD is purely controlled by nanoparticle diffusion through the porous matrix without the necessity of overcoming intermolecular forces between the component polymeric species.

3.4. Assessment of the size and stability of the CAP nanoparticles

A nanoparticle *z*-average size of 1654 and 241 nm was recorded for preliminary DA-free and DA-loaded CAP nanoparticles, respectively. The result was atypical as it was expected that the DA-free CAP nanoparticles would have a smaller size in comparison to the DA-loaded particles due to the absence of drug. However, the zeta potential of DA-loaded CAP nanoparticles displayed increased stability in comparison to the DA-free particles. DA-free particles therefore aggregated more easily, contributing to the relative increase in size. A polydispersity index (PdI) value of 0.030 was calculated for the DA-loaded CAP nanoparticles indicating minimal variation in particle size and highlighting the uniformity of particle size. Zeta potential values of −23.1 and −35.2 mV were recorded for DA-free and DA-loaded CAP nanoparticles respectively. While this result was indicative of the desirable lack of particle agglomeration in both DA-free and DA-loaded particles, it also revealed that the DA-loaded CAP nanoparticles displayed superior stability in comparison to DA-free particles. Fig. 5 depicts typical size and zeta potential intensity profiles generated.

3.5. Componential thermal analysis on the NESD

TMDSC profiles portrayed the paradigms of the thermal behavior in the three componential elements of the NESD that included the CAP nanoparticles, the crosslinked alginate scaffold and the assimilated NESD as shown in Fig. 6a–c. The changes in T_g, T_m and T_c
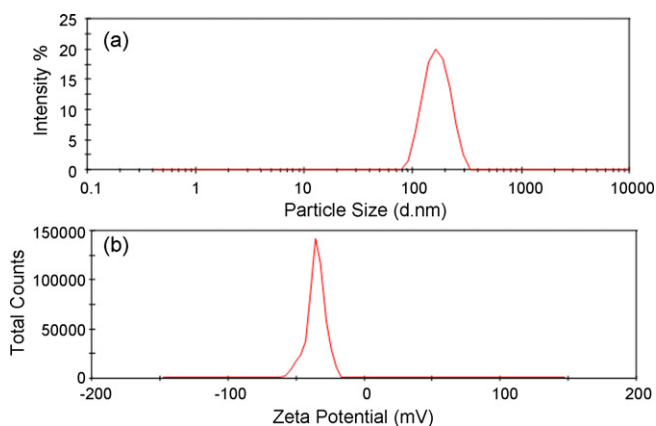
Fig. 5. Typical intensity profiles obtained showing (a) a size distribution profile, and (b) a zeta potential distribution profile of DA-loaded CAP nanoparticles.

that occurred upon the formation of DA-loaded CAP nanoparticles, the crosslinked alginate scaffold and the assimilated NESD when compared to native CAP employed for nanoparticle formation is depicted in Fig. 6a–c.

All components presented with triple exothermic peaks depicting a similarity in crystallization behaviors (T_c) (Fig. 6a–c). The similarity in thermal behavior between the crosslinked alginate scaffolds and NESD portrayed a direct indication of the high degree of crystallinity imparted by the secondary crosslinker $BaCl_2$ that was employed as a curing step for scaffold formation. Noteworthy was the significantly large variation in T_g and T_m between the native CAP ($T_g = 160–170\,°C$; $T_m = 192\,°C$) and the DA-loaded CAP nanoparticles ($T_g = 260\,°C$; $T_m = 268\,°C$). The apparent shifts in T_g and T_m elucidated a possible interfacing between CAP and DA molecules that contributed to the formation of physical interactions culminating in the thermal behavior observed. The large positive shifts in thermal events may have also influenced the release of DA from the CAP nanoparticles, indicative of the identified intermolecular association between DA and CAP, which serves to control drug release. This observation is supported by the initial prototyping technology employed and DA release profiles discussed later on. The presence of transient melting endothermic peaks and further shifts in T_g observed on the TMDSC signals of the NESD samples clearly reflected the effect of altered thermal properties produced by initial crosslinking between $[HOCH_2(CHOH)_4COO]_2Ca$ and alginate and further the dispersion of DA-loaded CAP nanoparticles within the $BaCl_2$ solution as a post-curing process. The altered thermal behavior influenced the physicomechanical behavior as supported by the
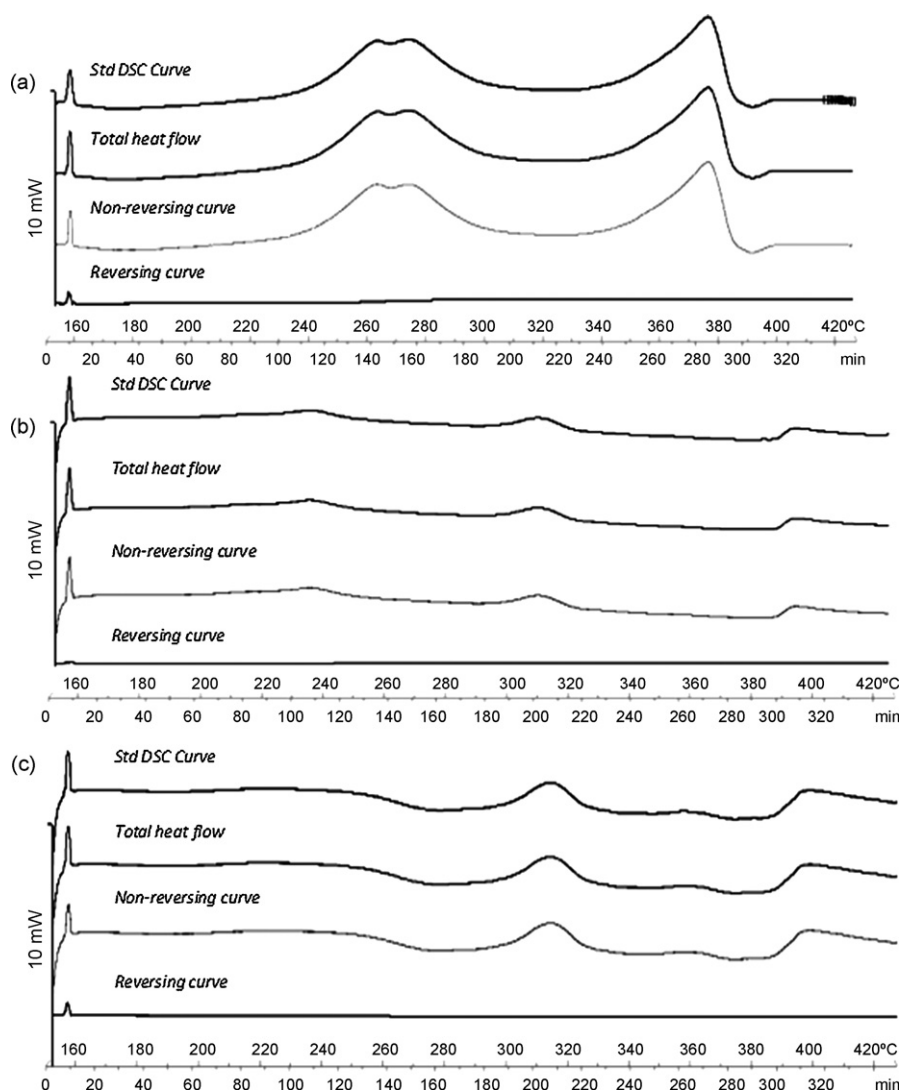

Fig. 6. TMDSC profiles generated for the (a) DA-loaded CAP nanoparticles, (b) crosslinked alginate scaffold and (c) the NESD.

earlier morphological, textural profile and FTIR analysis. Overall, the thermal behavior observed may be due to variation in the ΔH involved, ability to attain near-equilibrium conditions during measurement, and the rapid rate of change in molecular rearrangement compared to the ΔT. These pertinent intermolecular interactions, which resulted in the observed thermal transitions (Fig. 6a–c), may have also contributed substantially to the superior control of DA released from the NESD.

3.6. Drug entrapment efficiency within the CAP nanoparticles

The highest average drug entrapment efficiency (DEE) value of $63 \pm 0.35\%$ was computed for DA-loaded nanoparticles with a 10:1 polymer:drug ratio. This was considerably high in comparison to the lower polymer concentrations (5:1) used for nanoparticle formulation. Higher polymer concentrations were not used as it negatively impacted on the inherent physical stability of nanoparticle formation. The DEE value obtained was desirable for a nanoparticle formulation which exhibits a large surface area, and in particular for a highly water-soluble molecule such as DA. This is purportedly due to the affinity of DA for CAP, as predicted via molecular structural interactions, thereby increasing the DEE value.

3.7. Statistical response surface analysis

3.7.1. Analysis of Matrix Resilience of the crosslinked alginate scaffold

An increased scaffold Matrix Resilience (MR) was observed at higher alginate (2–3%, w/v) and $[HOCH_2(CHOH)_4COO]_2Ca$ concentrations (0.3–0.4%, w/v) (Fig. 7a). This was expected as at higher alginate concentrations (3%, w/v) an advanced degree of crosslinking occurred and produced a superiorly robust and interconnected polymeric networked structure with the increased availability of $[HOCH_2(CHOH)_4COO]_2Ca$. Higher processing temperatures (60–70 °C) and lower concentrations of alginate (1%, w/v) also provided a desirable MR value (Fig. 7b). This was attributed to the enhanced molecular mobility of alginate polymeric chains at higher temperatures (70 °C) that induced participation in the crosslinking reaction resulting in the preferred micromechanical behavior. The concentration of $[HOCH_2(CHOH)_4COO]_2Ca$ had the most significant effect in terms of achieving superior MR ($p \leq 0.05$) with increased concentrations providing higher MR values (>87.5%), while the processing temperature displayed the most significant role in matrix design ($p \leq 0.05$). A processing temperature of 50 °C also provided desirable MR values in the region of 85%. However this was not relevant for post-curing times of 60 min.

3.7.2. Analysis of Matrix Erosion of the crosslinked alginate scaffold

An increase in alginate concentration (2–3%, w/v) resulted in a reduced scaffold Matrix Erosion (ME) (Fig. 7c) as a result of a superiorly compact scaffold produced from a precursor solution of increased viscosity. Furthermore an increase in $[HOCH_2(CHOH)_4COO]_2Ca$ resulted in a greater degree of crosslinking thereby increasing the scaffold rigidity and retarding ME (84%). An increase in processing temperature (60–70 °C) and post-curing time (60–90 min) also retarded the ME (85%) as compared to >90% when lower post-curing times were used (40–50 min). Higher temperatures enhanced the aqueous solubility of $[HOCH_2(CHOH)_4COO]_2Ca$ and a prolonged post-curing
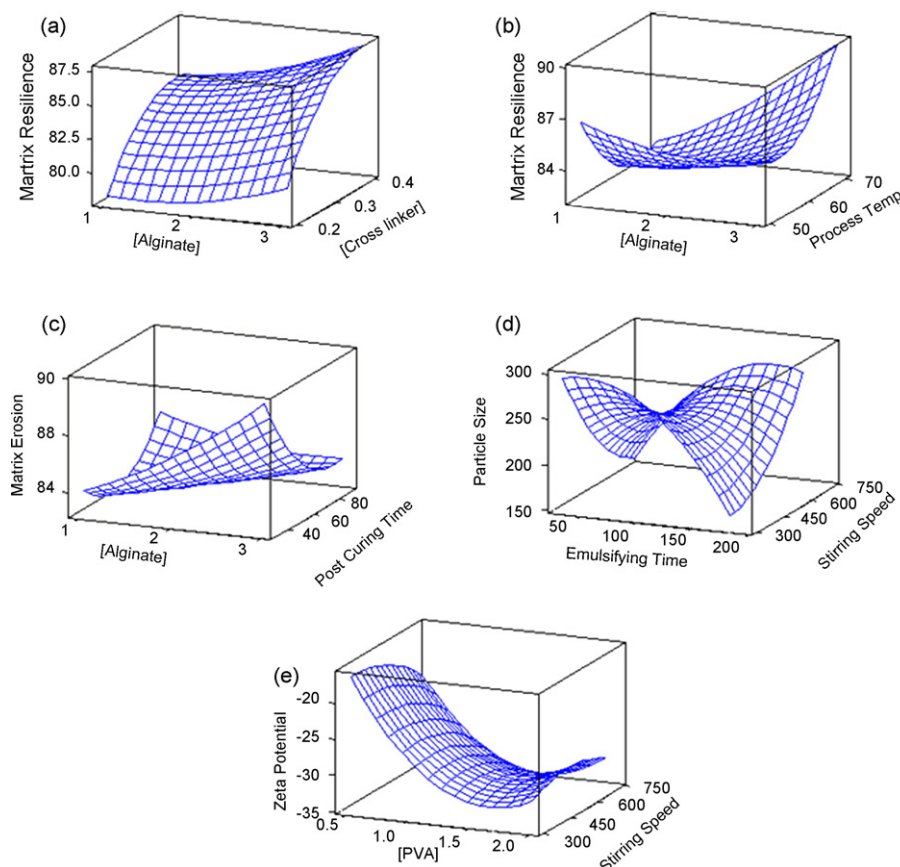

Fig. 7. Response surface plots correlating (a) Matrix Resilience with alginate and crosslinker concentration, (b) Matrix Resilience with alginate concentration and processing temperature, (c) Matrix Erosion with alginate concentration and post-curing time, (d) Particle Size with emulsifying time and stirring speed and (e) Zeta Potential with PVA concentration and stirring speed (note: $p \leq 0.05$ in all cases).

period allowed for optimal crosslinking and subsequently controlling the rate and extent of ME. Furthermore an increase in $[HOCH_2(CHOH)_4COO]_2Ca$ concentration facilitated ME ($p \geq 0.05$). This was unexpected and may have resulted from an excess in free $[HOCH_2(CHOH)_4COO]_2Ca$ ions present at the saturation point that initiated auto-catalysis and the rapid dissolution of the highly water soluble crosslinker from the scaffold thus increasing the scaffold ME. A higher processing temperature coupled with a decreased alginate concentration also retarded the ME ($p \leq 0.05$). At higher processing temperatures further uniformity and efficiency in the distribution of alginate became apparent within the scaffold matrix thereby contributing to the superiorly controlled ME dynamics.

3.7.3. Analysis of mean dissolution time of the DA-loaded CAP nanoparticles

The altering DA release profiles for the respective CAP nanoparticulate formulations formulated as per the Box–Behnken design template and from the optimally defined NESD in simulated CSF signified the ability to flexibly modulate the release of DA from the CAP nanostructures. A prominent interaction described by discontinuous aggregation and subsequent clustering between the predominant polymers CAP and PVA was noted. An increase in CAP concentration (0.75–1%, w/v) and a decrease PVA concentration (0.5%, w/v) led to a higher MDT value and vice versa. An increase in PVA concentration (1.5–2%, w/v) was able to control and limit DA release. Lower stirring speeds (300 rpm) also yielded nanoparticles displaying higher MDT values (41.75) presumably due to the enablement of an enhanced drug–polymer interaction with more efficient entrapment of DA within the CAP, and a resultant enhanced control over DA release, when subjected to reduced shear rates.

3.7.4. Analysis of particle size of the DA-loaded CAP nanoparticles

Fig. 7d revealed that an increase in stirring speed (600–750 rpm) had an uncharacteristic and unfavorable effect on particle size with particles produced within a larger size range of 250–300 nm. A prolonged emulsification phase of between 150 and 180 min coupled with a desirable lower stirring speed (300–450 rpm) resulted in the formation of dispersed non-aggregated particles with a reduced particle size of ~200 nm (Fig. 7d). An interesting observation was that a decrease in CAP concentration (0.5%, w/v) resulted in increased particle sizes ranging from 200 to 225 nm. DEE results obtained from the experimental design template demonstrated that a significantly lower DEE was achieved with an increase in CAP concentration which may have resulted in decreased particle sizes. The concentration of PVA was also influential in terms of particle size, with particle sizes increasing with an increase in PVA concentration coupled with higher stirring speeds ($p \leq 0.05$). A lower concentration of PVA employed at a reduced agitation rate was sufficient to ensure the homogenous impartation of surfactant properties to the formulation thereby reducing the risk of particle attraction that could produce unfavorably larger particle sizes.

3.7.5. Analysis of zeta potential of the DA-loaded CAP nanoparticles

An increase in PVA concentration (1.5–2%, w/v) provided desirable zeta potential values ranging from −30 to −35 mV (Fig. 7e). This was attributed to the ability of PVA to act as an absorptive surfactant that decreased the interfacial tension and thus imparted stability to the nanoparticles ($p \leq 0.05$). A distinct relationship between lower PVA concentrations and suitable zeta potential values was noted in consideration of the physical interaction between CAP and PVA.

3.8. Constrained optimization of NESD formulation responses

Optimization of the NESD was performed employing Minitab® V15 statistical software (Minitab® Inc., PA, USA) to determine the optimum level for each variable for both the crosslinked alginate scaffold and DA-loaded CAP nanoparticles. The optimization process resulted in the attainment of formulations with a considerably low desirability value for all three outcomes ($D_{optimal} < 1$). Thus a selective approach based on the most influential desired outcome was used. The Matrix Resilience and Matrix Erosion were the most significant characteristics optimized for the crosslinked alginate scaffold ($p < 0.05$). Maximization of the Matrix Resilience would ensure that premature collapse of the lyophilized device would not occur and minimization of the Matrix Erosion would facilitate the prolonged and controlled delivery of DA to the brain. The MDT value for the CAP nanoparticles was further controlled by the incorporation of the DA-loaded CAP nanoparticles within the crosslinked alginate scaffold. The CAP nanoparticles having the smallest particle size (≈ 200 nm) for facilitation of diffusion through the alginate scaffold, with high desirability (>99%) was selected as the optimal nanoparticle formulation. Residual analysis of the scaffold Matrix Resilience, Matrix Erosion, the MDT values of the nanoparticle formulations, particle size and zeta potential showed the random distribution of data. Normal residual plots displayed insignificant profile curvature due to a reduction in observation points (<50), however maintained normality for the scaffold optimization. The residual plots for CAP nanoparticle optimization were distinctly linear with normality ($R^2 = 0.98$). Residual versus fitted plots displayed data randomness along the baseline residual value of 0 within three standard deviations of the mean. Furthermore, no expression of blueprinting was indicative of a trendless circumstance. This was supported by histograms depicting the residuals having a normal distribution with a zero mean and a constant variance. Non-random error identification plots revealed typical positive (clustering of formulations 4–12) and negative correlation indicated by rapid changes in the signs (−/+) of the consecutive residuals.

3.9. Desirability analysis for the measured responses of the optimized NESD

With reference to the optimized crosslinked alginate scaffold, the Matrix Resilience of the experimental formulation (82.46%) displayed favorability to the fitted formulation (88.98%). While the experimental formulation had a slightly lower Matrix Resilience than the fitted, this was counteracted by the Matrix Erosion which was lower than predicted (only 18.23% after 7 days). The optimized NESD formulation proved to have the desired characteristics of increased Matrix Resilience and a decreased Matrix Erosion. For the optimized DA-loaded CAP nanoparticles, the MDT value desirability of 94.41% was the most promising outcome and therefore DA release from the CAP nanoparticles were controlled and sustained for the period of time desired. With reference to the particle size (possessing a statistical desirability of 76.15%); while the value of 197 nm was not ideal for the optimally specified system, it was within the limits set for pharmaceutical nano-therapeutic systems of <200 nm and would possess the propensity to diffuse through the scaffold pores (Farokhzad and Robert Langer, 2006). The desirability value of 76.68% obtained for the zeta potential optimization signified that it differed substantially from the fitted value with a superior value in terms of stability of −34.00 mV for the optimized system. Overall, the optimized system displayed the desirable DA release, size and stability required for utilization as an intracranial device for the prolonged and controlled delivery of DA to the brain tissue.
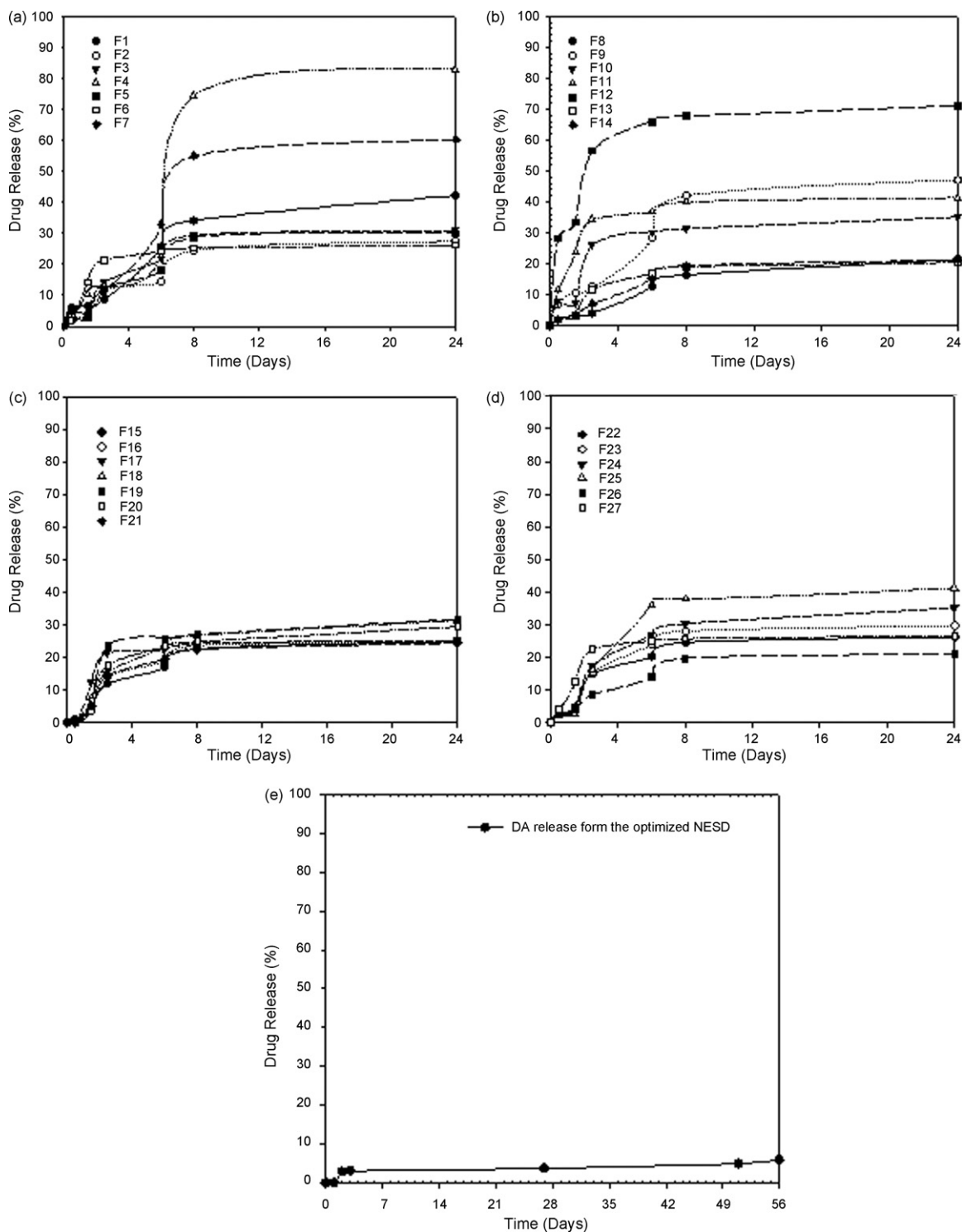
Fig. 8. Drug release profiles of (a–d) DA released from CAP nanoparticles formulated as per the Box–Benken design template and (e) DA released from the optimally defined NESD in simulated cerebrospinal fluid, PBS (pH 6.8; 37 °C) over 56 days.

3.10. In vitro DA release from the NESD

The release of DA from the NESD (Fig. 8) displayed an initial lag phase compared to the CAP nanoparticles which were not configured within the crosslinked alginate scaffold. The mechanically patent and interconnected crosslinked alginate scaffold aided in reducing the initial burst effect of DA. The controlled migration of the CAP nanoparticles from the porous scaffold to the diffusional environment ultimately served to modulate the release of DA at the site of implantation.

3.11. In vivo analysis of DA release from the NESD in the Sprague–Dawley rat model

The generic SPE procedure selected in order to isolate DA from the plasma and CSF samples was suitable for retaining the polar DA
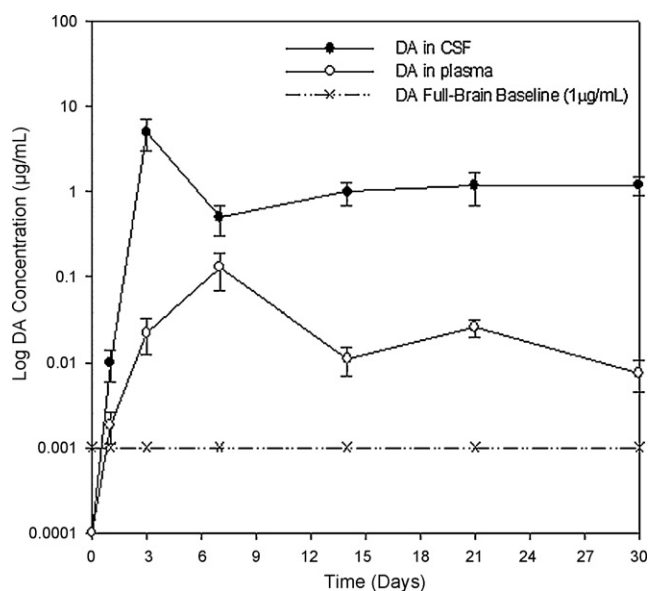
Fig. 9. Deconvoluted *in vivo* profiles of DA released in plasma and cerebrospinal fluid from the NESD device.

compound. Serial dilutions of methanol solutions ranging from 5 to 100% (v/v) with either the addition of acetic acid or sodium hydroxide were employed in the SPE procedure. It was noted that during the acidic phase (CH_3COOH) higher integral UPLC peaks and extraction yields were obtained as compared to the basic phase (NaOH), in particular, at 70% (v/v) methanol with 2% (v/v) acetic acid. An additional wash-step of 45% (v/v) methanol produced even larger recoveries and level chromatographic baselines. The extraction recoveries ranged from 95.89 to 101.02%, while the precision values ranged from 3.5 to 11.7% over three concentrations evaluated over three consecutive days. Results indicated that the implemented SPE and assay procedure displayed acceptable accuracy and precision ($R^2 = 0.99$).

DA release from the NESD was assessed over a period of 30 days (Fig. 9). The DA release from the NESD produced a peak at 3 days in both the CSF and plasma, the CSF concentration of DA representing 28% of the total DA incorporated within the NESD, while the plasma concentration was only 1.2% of the total concentration present within the CSF. The pharmacokinetic profile for plasma showed low levels of DA release throughout the 30 days of the study whereas the CSF concentration of DA peaked at 3 days and thereafter reached a plateau that maintained DA levels over the investigational period. Low levels of DA release can be favorably considered, due to minimization of CNS side-effects.

The normal DA levels in the Sprague–Dawley rat are 10.9 and 0.58 μg/mL in the striatum corneum and the rest of the brain respectively. The total baseline concentration of DA in the full brain has been reported as 0.98 μg/mL (Hutson and Curzon, 1989). At the plateau phase, the DA concentration in the CSF achieved by the NESD was 11.0 μg/mL after consideration of the inherent baseline concentration of DA in the Sprague–Dawley rat brain model from plasma samples taken at t_{0h}. The device can thus be considered to maintain an adequate level of DA within the brain over the 30-day period. Furthermore, the NESD demonstrated minimal bioerosion (26%) following recovery from the frontal lobe parenchyma at 30 days. Cytotoxic studies on the NESD following 3-(4,5-dimethylthiazol-2-yl)-2,5-diphenyltetrazolium bromide (MTT) assays on white blood cells and human carcinomic SK-N-MC cell lines did not display any noteworthy unfavorable effects on cell survival and growth (data not shown here).

Overall, the NESD was implanted at the site of action and therefore substantially improved the delivery of DA to the brain. In addition, DA concentrations in the plasma were minimal and therefore could culminate in a drastically reduced side-effects profile compared to orally administered levodopa preparations due to peripheral conversion of levodopa to dopamine.

4. Conclusions

The DEE of DA within the CAP nanoparticles was relatively high and compensated for the rapid *in vitro* release of DA from the nanoparticles. SEM and TEM images further established the uniformity and sphericity of the DA-loaded CAP nanoparticles with FTIR analysis revealing the presence of both CAP and DA within the nanoparticles. Zetasize analysis confirmed the stability of the nanoparticles within the desirable nano-size range. Significant shifts in thermal events noted with TMDSC analysis of the DA-loaded CAP nanoparticles and NESD supported the mechanism by which modulated release of DA occurred from the device as a result of polymorphic transitions of the crosslinked scaffold that further controlled the outward diffusion of the CAP nanoparticles. Biometric simulation and prototyping technology in conjunction with Box–Behnken statistical experimental designs as preparation and optimization strategies for the scaffold and nanoparticles proved robust in selecting optimal components for assembling the NESD. *In vitro* and *in vivo* DA release confirmed that the NESD provided higher levels and controlled delivery of DA in the CSF of the Sprague–Dawley rat model and thus may serve as a desirable platform for the site-specific delivery of DA for the chronic management of Parkinson's disease. Further optimization of the NESD with respect to ease of implantation and bioadhesion will be undertaken in future investigations, in addition to more extended studies in the Sprague–Dawley rat model to identify the frequency of implantation of the NESD device.

Ethical approval

References

Ahmad, F.J., Khan, R.K., 2005. Nanotechnology: a revolution in the making. Pharm. Rev. 75, 801–802.

Bilensoy, E., 2007. Tumor targeted nanoparticles for cancer therapy. Eur. J. Pharm. Sci. 32, S10.

Cheah, C.M., et al., 2002. Characterization of microfeatures in selective laser sintered drug delivery devices. Proc. Inst. Mech. Eng. Part H: J. Eng. Med. 216, 369–383.

Chen, J.J., Obering, C., 2005. A review of intermittent subcutaneous apomorphine injections for the rescue management of motor fluctuations associated with advanced Parkinson's disease. Clin. Ther. 27, 1710–1724.

Chua, C.K., et al., 2000. Fabricating facial prosthesis models using rapid prototyping tools. Integr. Manuf. Syst. (Int. J. Manuf. Technol. Manage.) 11, 42–53.

Curodeau, A., Sachs, E., Caldarise, S., 2000. Design and fabrication of cast orthopedic implants with freeform surface textures from 3D printed ceramic shell. J. Biomed. Mater. Res. 53, 525–535.

Discher, D.E., Ortiz, V., Srinivas, G., Klein, M.L., Kim, Y., Christian, D., Cai, S., Photos, P., Ahmed, F., 2007. Emerging applications of polymersomes in drug delivery: from molecular dynamics to shrinkage of tumors. Prog. Polym. Sci. 32, 838–857.

Elkharraz, K., Faisant, N., Guse, C., Siepmann, F., Arica-Yegin, B., Oger, J.M., Gust, J., Goepferich, A., Benoit, J.P., Siepmann, J., 2006. Paclitaxel-loaded microparticles and implants for the treatment of brain cancer: preparation and physicochemical characterization. Int. J. Pharm. 314, 127–136.

Farokhzad, O.C., Robert Langer, R., 2006. Nanomedicine: developing smarter therapeutic and diagnostic modalities. Adv. Drug Deliv. Rev. 58, 1456–1459.

Ferrero, M.C., Velasco, M.V., Ford, J.L., Rajabi-Siahboomi, A.R., Muñoz, A., Jiménez-Castellanos, M.R., 1999. Determination of glass transition temperatures of some new methyl methacrylate copolymers using modulated temperature differential scanning calorimetry (MTDSC). Pharm. Res. 16, 1464–1469.

Hall, V.J., Li, J., Brundin, P., 2007. Restorative cell therapy for Parkinson's disease: a quest for the perfect cell. Semin. Cell Dev. Biol. 18, 859–869.

Hely, M.A., Fung, V.S.C, Morris, J.G.L., 2000. Treatment of Parkinson's disease. J. Clin. Sci. 7, 484–494.

Hutson, P.H., Curzon, G., 1989. Concurrent determination of effects of p-chloroamphetamine on central extracellular 5-hydroxytryptamine concentration and behaviour. Br. J. Pharm. 96, 801–806.

Levy, R.A., et al., 1997. CT-generated porous hydroxyapatite orbital floor prosthesis as a prototype bioimplant. Am. J. Neuroradiol. 18, 1522–1525.

Liu, T.X., Liu, Z.H., Ma, K.X., Shen, L., Zeng, K.Y., He, C.B., 2003. Morphology, thermal and mechanical behavior of polyamide 6/layered-silicate nanocomposites. Comp. Sci. Technol. 63, 331–337.

Marin, C., Aguilar, E., Mengod, G., Cortes, R., Rodriguez-Oroz, M.C., Obeso, J.A., 2008. Entacapone potentiates the long-duration response but does not normalize levodopa-induced molecular changes. Neurobiol. Dis. 32, 340–348.

Ono, I., et al., 1999. Treatment of large complex cranial bone defects by using hydroxyapatite ceramic implants. Plastic Reconstr. Surg. 104, 339–349.

Pahwa, R., Koller, W.C., 1998. Advances in the treatment of Parkinson's disease. Drugs Today 34, 95.

Papapetropoulos, S., Mash, D.C., 2005. Psychotic symptoms in Parkinson's disease: from description to etiology. Neurology 252, 753–764.

Piñón-Segundo, E., Ganem-Quintana, A., Alonso-Pérez, V., Quintanar-Guerrero, D., 2005. Preparation and characterization of triclosan nanoparticles for periodontal treatment. Int. J. Pharm. 294, 217–232.

Poletto, F.S., Fiel, L.A., Donida, B., Re, M.I., Guterres, S.S., Pohlmann, A.R., 2008. Controlling the size of poly(hydroxybutyrate-co-hydroxyvalerate) nanoparticles prepared by emulsification–diffusion technique using ethanol as surface agent. Colloid Surf. A: Physicochem. Eng. Aspects, 105–112.

Porter, N.L., Pilliar, R.M., Grynpas, M.D., 2001. Fabrication of porous calcium polyphosphate implants by solid freeform fabrication: a study of processing parameters and in vitro degradation characteristics. J. Biomed. Mater. Res. 56, 504–515.

Reading, M., 1993. Modulated differential scanning calorimetry—a new way forward in materials characterization. Trends Polym. Sci. 1, 248–253.

Redhead, M., Davis, S.S., Illum, L., 2001. Drug delivery in poly(lactide-co-glycolide) nanoparticles surface modified with poloxamer 407 and poloxamine 908: in vitro characterization and in vivo evaluation. J. Control. Release 70, 353–363.

Roos, R.A.C., Tijssen, M.A.J., Van der Velde, E.A., Breimer, D.D., 1993. The influence of a standard meal on Sinemet® CR absorption in patients with Parkinson's disease. Clin. Neurol. Neurosurg. 95, 215–219.

Samii, A., Nutt, J.G., Ransom, B.R., 2004. Parkinson's disease. Lancet 363, 1783–1793.

Sandor, M., Bailey, N.A., Mathiowitz, E., 2002. Characterization of polyanhydride microsphere degradation by DSC. Polymer 43, 279–288.

Singh, N., Pillay, V., Choonara, Y.E., 2007. Advances in the treatment of Parkinson's disease. Prog. Neurobiol. 81, 29–44.

Uitti, R.J., Vingerhoets, F.J.G., Hayward, M., Cooper, S., Snow, B.J., 1997. Positron emission tomography (PET) measurements of striatal D_2 receptors in untreated Parkinson's disease patients with follow-up after 6 and 12 months' treatment with Sinemet® or Sinemet® CR. Parkinson's Related Disorders 3, 43–46.

Whitney, C.M., 2007. Medications for Parkinson's disease: patient and family fact sheet. Neurologist 13, 387–388.